Wakefield generation and GeV acceleration in tapered plasma channels

P. Sprangle,[1] B. Hafizi,[2] J. R. Peñano,[3] R. F. Hubbard,[1] A. Ting,[1] C. I. Moore,[1] D. F. Gordon,[4] A. Zigler,[5] D. Kaganovich,[5] and T. M. Antonsen, Jr.[6]

[1]*Plasma Physics Division, Naval Research Laboratory, Washington, DC 20375*

[2]*Icarus Research, Inc., P.O. Box 30780, Bethesda, Maryland 20824-0780*

[3]*LET Corporation, 4431 MacArthur Boulevard, Washington, DC 20007*

[4]*Naval Research Laboratory, National Research Council, Washington, DC 20375*

[5]*Hebrew University, Jerusalem, Israel*

[6]*University of Maryland, College Park, Maryland 20742*

(Received 20 September 2000; revised manuscript received 22 November 2000; published 18 April 2001)

To achieve multi-GeV electron energies in the laser wakefield accelerator (LWFA), it is necessary to propagate an intense laser pulse long distances in a plasma without disruption. One of the purposes of this paper is to evaluate the stability properties of intense laser pulses propagating extended distances (many tens of Rayleigh ranges) in plasma channels. A three-dimensional envelope equation for the laser field is derived that includes nonparaxial effects such as group velocity dispersion, as well as wakefield and relativistic nonlinearities. It is shown that in the broad beam, short pulse limit the nonlinear terms in the wave equation that lead to Raman and modulation instabilities cancel. This cancellation can result in pulse propagation over extended distances, limited only by dispersion. Since relativistic focusing is not effective for short pulses, the plasma channel provides the guiding necessary for long distance propagation. Long pulses (greater than several plasma wavelengths), on the other hand, experience substantial modification due to Raman and modulation instabilities. For both short and long pulses the seed for instability growth is inherently determined by the pulse shape and not by background noise. These results would indicate that the self-modulated LWFA is not the optimal configuration for achieving high energies. The standard LWFA, although having smaller accelerating fields, can provide acceleration for longer distances. It is shown that by increasing the plasma density as a function of distance, the phase velocity of the accelerating field behind the laser pulse can be made equal to the speed of light. Thus electron dephasing in the accelerating wakefield can be avoided and energy gain increased by spatially tapering the plasma channel. Depending on the tapering gradient, this luminous wakefield phase velocity is obtained several plasma wavelengths behind the laser pulse. Simulations of laser pulses propagating in a tapered plasma channel are presented. Experimental techniques for generating a tapered density in a capillary discharge are described and an example of a GeV channel guided standard LWFA is presented.

DOI: 10.1103/PhysRevE.63.056405 PACS number(s): 52.35.Mw, 41.75.Jv, 52.50.−b

I. INTRODUCTION

The extremely large acceleration gradients generated by laser pulses propagating in plasmas can be used to accelerate electrons [1–7]. In the standard laser wakefield accelerator (LWFA) a short laser pulse, on the order of a plasma wavelength long, excites a trailing plasma wave that can trap and accelerate electrons to high energy. There are a number of issues that must be resolved before a viable, practical high-energy accelerator can be developed. These include Raman, modulation, and hose instabilities that can disrupt the acceleration process [8–16]. In addition, extended propagation of the laser pulse is necessary to a achieve high electron energy. In the absence of optical guiding the acceleration distance is limited to a few Rayleigh ranges, which is far below that necessary to reach GeV electron energies [1,17]. The physics of laser beams propagating in plasmas has been studied in great detail [8,18–23], and there is ample experimental confirmation of extended guided propagation in plasmas and plasma channels [24–30]. In addition to these issues, dephasing of electrons in the wakefield can limit the energy gain. Spatially tapering the plasma density may be useful in overcoming electron dephasing in the wakefield.

This paper addresses the guiding and stability of an intense laser pulse in a uniform plasma channel and analyzes the wakefield acceleration process in an inhomogeneous channel. The coupled electromagnetic and plasma wave equations are derived for laser pulses propagating in a plasma channel with a parabolic radial density profile and arbitrary axial density variation. For a uniform channel, Raman and modulation instabilities are analyzed and numerical solutions of the three-dimensional (3D) wave equation are discussed. In particular, propagation of short laser pulses over many Rayleigh ranges is demonstrated for a uniform channel. For a nonuniform channel the axial and radial electric fields associated with the plasma wave are obtained inside and behind the laser pulse. It is shown analytically and through numerical simulations that by tapering the plasma density the wakefield phase velocity several plasma wavelengths behind the laser pulse can equal the speed of light *in vacuo*. Tapered density channels have been produced experimentally in capillary discharges, and optical guiding in these channels has been demonstrated. A variable channel density may be generated by tapering the wall radius of the capillary [27], or by applying different voltages to a segmented capillary.

The equations for the laser envelope and wakefield are derived in Sec. II. The formulation includes the effects of plasma density inhomogeneity, diffraction, nonparaxial

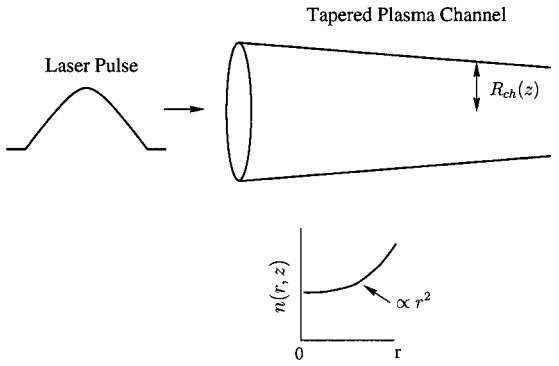

FIG. 1. Schematic showing a laser pulse entering an axially tapered plasma channel having a parabolic radial density profile.

propagation, dispersion, and nonlinearities arising from plasma waves and relativity. The propagation of laser pulses in a uniform plasma channel is analyzed and discussed in Sec. III. Instabilities resulting in Raman scattering and modulation of the laser pulse are also discussed. Numerical results illustrating pulse propagation in three dimensions are presented in Sec. IV. In Sec. V an example of a GeV wakefield accelerator in a plasma channel is discussed. Laser wakefield generation and acceleration in a tapered plasma channel is the subject of Sec. VI. Section VI also discusses the experimental realization of a tapered plasma channel. A summary of the results is given in Sec. VII.

II. LASER AND PLASMA WAVE EQUATIONS

In this section an envelope equation for a linearly polarized laser pulse propagating in a spatially tapered plasma channel, as shown in Fig. 1, is obtained. The wave equation for the laser electric field $\mathbf{E}(r,z,t)$ in a tapered channel, correct to order $|\mathbf{E}|^3$, is given by [8]

$$\left(\nabla^2-\frac{1}{c^2}\frac{\partial^2}{\partial t^2}\right)\mathbf{E}=\frac{\omega_p^2(z)}{c^2}\left(1+\frac{r^2}{R_{\rm ch}^2(z)}+\frac{\delta n}{n_0(z)}-\frac{|a|^2}{4}\right)\mathbf{E}, \tag{1}$$

where $\omega_p(z)=[4\pi e^2 n_0(z)/m]^{1/2}$ is the plasma frequency, $n_0(z)$ is the nonuniform plasma channel density, $R_{\rm ch}(z)$ is the channel radius associated with the parabolic density profile, δn is the plasma density perturbation associated with the wakefield, $|a|=(|e|/mc\omega_0)\langle 2\mathbf{E}\cdot\mathbf{E}\rangle^{1/2}$ is the magnitude of the electron oscillation momentum normalized to mc, and the brackets denote a time average. The first three terms on the right hand side of Eq. (1) represent, respectively, the parabolic plasma density channel, the plasma wakefield, and the relativistic mass correction.

The electric field associated with the wakefield $\mathbf{E}_p(r,z,t)$ in spatially tapered plasma is given by

$$\left(\frac{\partial^2}{\partial t^2}+\omega_p^2(z)\right)\mathbf{E}_p=-\frac{mc^2}{|e|}\frac{\omega_p^2(z)}{4}\nabla|a|^2, \tag{2}$$

where the perturbed wakefield density perturbation is given by

$$\frac{\delta n}{n_0(z)}=\frac{-|e|}{m\omega_p^2(z)}\nabla\cdot\mathbf{E}_p. \tag{3}$$

Equation (2) is correct to lowest order in a^2, and has been derived for a spatially varying plasma density, i.e., ω_p is a function of z.

The laser electric field can be written in terms of a slowly varying envelope and a rapidly varying phase

$$\mathbf{E}(r,z,t)=\tfrac{1}{2}(mc\omega_0/|e|)a(r,z,t)\times\exp\left[i\left(\int_0^z k_0(z)dz-\omega_0 t\right)\right]\hat{\mathbf{e}}_\perp+\text{c.c.}, \tag{4}$$

where $a(r,z,t)$ is proportional to the complex field amplitude, i.e., approximately equal to the normalized vector potential ($|a|$ is approximately equal to the electron oscillation momentum normalized to mc), $k_0(z)$ is the wave number, ω_0 is the carrier frequency, $\hat{\mathbf{e}}_\perp$ is a transverse unit vector, c.c. denotes the complex conjugate, and $\langle\mathbf{E}\cdot\mathbf{E}\rangle=(mc\omega_0/e)^2|a|^2/2$. Substituting the above field representation into Eq. (1) yields the following envelope equation:

$$\left(\nabla_\perp^2-k_0^2+\frac{\omega_0^2}{c^2}+i\frac{\partial k_0}{\partial z}+2ik_0\frac{\partial}{\partial z}+2i\frac{\omega_0}{c^2}\frac{\partial}{\partial t}+\frac{\partial^2}{\partial z^2}-\frac{1}{c^2}\frac{\partial^2}{\partial t^2}\right)a(r,z,t)=\frac{\omega_p^2}{c^2}\left(1+\frac{r^2}{R_{\rm ch}^2}+\frac{\delta n}{n_0}-\frac{|a|^2}{4}\right)a(r,z,t). \tag{5}$$

In Eq. (5), it is convenient to change independent variables from z,t to z,τ, where $\tau=t-\int_0^z dz'/v_g(z')$. In terms of the new variables, $\partial/\partial t\to\partial/\partial\tau$, $\partial/\partial z\to\partial/\partial z-[1/v_g(z)]\partial/\partial\tau$, and the laser envelope equation becomes

$$\left[\nabla_\perp^2+\frac{4}{r_o^2}-\frac{\omega_p^2}{c^2}\frac{r^2}{R_{\rm ch}^2}+\Delta k^2+2ik_0\left(1+\frac{i}{k_0v_g}\frac{\partial}{\partial\tau}\right)\frac{\partial}{\partial z}+i\frac{\partial k_0}{\partial z}\left(1-\frac{i}{k_0v_g}\frac{\partial}{\partial\tau}\right)+2i\left(\frac{\omega_0}{c^2}-\frac{k_0}{v_g}\right)\frac{\partial}{\partial\tau}+v_g^{-2}(1-\beta_g^2)\frac{\partial^2}{\partial\tau^2}+\frac{\partial^2}{\partial z^2}-\frac{\omega_p^2}{c^2}\left(\frac{\delta n}{n_0}-\frac{|a|^2}{4}\right)\right]a(r,z,\tau)=0, \tag{6}$$

where

$$\Delta k^2(z)=\frac{\omega_0^2}{c^2}-k_0^2(z)-\frac{\omega_p^2(z)}{c^2}-\frac{4}{r_0^2}.$$

In obtaining Eq. (6), the term $4/r_0^2$, where r_0 is the initial laser spot size, has been added and subtracted in order to

have finite transverse effects included in the expression for the linear group velocity. By defining the laser wave number and group velocity to be

$$k_0(z)=c^{-1}\sqrt{\omega_0^2-4c^2/r_0^2-\omega_p^2(z)} \tag{7a}$$

and

$$\nu_g(z)=c^2k_0(z)/\omega_0\,. \tag{7b}$$

respectively, Eq. (6) reduces to

$$\left[\nabla_\perp^2+\frac{4}{r_0^2}-\frac{\omega_p^2(z)}{c^2}\frac{r^2}{R_{\rm ch}^2(z)}+2ik_0(z)\left(1+\frac{i}{k_0(z)\nu_g(z)}\frac{\partial}{\partial\tau}\right)\frac{\partial}{\partial z}+i\frac{\partial k_0}{\partial z}\left(1-\frac{i}{k_0(z)\nu_g(z)}\frac{\partial}{\partial\tau}\right)+\nu_g^{-2}(z)\gamma_g^{-2}(z)\frac{\partial^2}{\partial\tau^2}-\frac{\omega_p^2(z)}{c^2}\left(\frac{\delta n}{n_0}-\frac{|a|^2}{4}\right)\right]a(r,z,\tau)=0, \tag{8}$$

where $\gamma_g=(1-\beta_g^2)^{-1/2}$ is the relativistic factor associated with the group velocity, $\beta_g=\nu_g/c$, and the small term proportional to $\partial^2/\partial z^2$ has been neglected. In Eq. (8), the group velocity dispersion (GVD) is represented by terms proportional to $\partial^2/\partial\tau^2$ and higher order τ derivatives, introduced through the $\partial^2/\partial\tau\partial z$ term [31].

III. PULSE PROPAGATION IN A UNIFORM PLASMA CHANNEL

We first consider the dynamics of a laser pulse propagating in an untapered plasma channel. For a uniform channel the envelope and wakefield density equations become

$$\left[\nabla_\perp^2+\frac{4}{r_0^2}-\frac{\omega_p^2}{c^2}\frac{r^2}{R_{\rm ch}^2}+2ik_0\left(1+\frac{i}{k_0\nu_g}\frac{\partial}{\partial\tau}\right)\frac{\partial}{\partial z}+\nu_g^{-2}\gamma_g^{-2}\frac{\partial^2}{\partial\tau^2}-\frac{\omega_p^2}{c^2}\left(\frac{\delta n}{n_0}-\frac{|a|^2}{4}\right)\right]a(r,z,\tau)=0, \tag{9a}$$

$$\left(\frac{\partial^2}{\partial\tau^2}+\omega_p^2\right)\frac{\delta n}{n_0}=\frac{c^2}{4}\nabla^2|a(r,z,\tau)|^2, \tag{9b}$$

where

$$\gamma_g=\omega_0/(\omega_p^2+4c^2/r_0^2)^{1/2}. \tag{10}$$

In the broad beam limit ($r_o\gg L$, where L is the pulse length), $\nabla^2\cong\partial^2/\partial z^2\cong c^{-2}\partial^2/\partial\tau^2$, and Eq. (9b) becomes

$$\left(\frac{\partial^2}{\partial\tau^2}+\omega_p^2\right)\frac{\delta n}{n_0}\cong\frac{1}{4}\frac{\partial^2|a|^2}{\partial\tau^2}. \tag{11}$$

In addition, for a short pulse, $L\ll\lambda_p$ we find from Eq. (11) that $\delta n/n_0\cong|a|^2/4$. In these limits the nonlinear terms, i.e., wakefield and relativistic terms, in Eq. (9a) cancel [32]. This implies that the Raman and modulation instability cancel each other out in these limits. The possibility that short laser pulses could propagate without instability was postulated in Ref. [1]. In addition, short pulses were shown to not undergo relativistic focusing in Ref. [32].

Pulse length envelope equation, pulse spreading, and. chirping

In the long pulse ($L\gg\lambda_p$), broad beam ($r_0\gg L$) limit it follows from Eq. (10) that $|\delta n/n_0|\approx O[(\lambda_p/L)^2,(\lambda_p/r_0)^2]|a|^2\ll|a|^2$. In this limit $\delta n/n_0$ can be neglected. For a matched beam, i.e., $r_0=(2cR_{\rm ch}/\omega_p)^{1/2}=$const [see Eq. (22)], and $\lambda/L\ll1$, Eq. (9a) reduces to

$$\left(\frac{\partial^2}{\partial\tau^2}-\frac{2i}{\beta_2}\frac{\partial}{\partial z}-\frac{\omega_p^2}{4k_0c^2\beta_2}|a(0,z,\tau)|^2\right)a(0,z,\tau)=0, \tag{12}$$

where

$$\beta_2=-\frac{1}{k_0\nu_g^2\gamma_g^2}\cong-\left(\frac{\omega_p^2+4c^2/r_0^2}{c\omega_0^3}\right), \tag{13}$$

is the GVD parameter. Note that β_2 is always negative for a plasma. Equation (12) is identical in form to the conventional paraxial wave equation containing a nonlinear focusing term, with the transverse coordinate replaced with τ. An equation describing the evolution of the pulse duration $\tau_0(z)$ can be obtained from Eq. (13) by taking $a(0,z,\tau)$ to have a Gaussian longitudinal profile, $\exp[-\tau^2/\tau_0^2(z)]$, where $L=c\tau_0(0)$. Substituting this profile into Eq. (12) and expanding the nonlinear term, $\exp[-2\tau^2/\tau_0^2(z)]\approx1-2\tau^2/\tau_0^2(z)$, and matching τ^2 terms, yields the following equation for the pulse duration:

$$\frac{\partial^2T_0(Z)}{\partial Z^2}-\frac{1}{T_0^3(Z)}\left(1+{\rm sgn}(\beta_2)\frac{I}{I_c}T_0^2(Z)\right)=0, \tag{14}$$

where $T_0(Z)=\tau_0(z)/\tau_0(0)$ is the normalized pulse duration, $Z=z/Z_{\rm GVD}$ is the normalized propagation distance, $Z_{\rm GVD}=\tau_0^2(0)/(2|\beta_2|)$ is the well known [31,33] dispersion distance (equivalent to a longitudinal Rayleigh length), $I=c\langle\mathbf{E}\cdot\mathbf{E}\rangle/4\pi=c(mc\omega_0/e)^2|a|^2/8\pi$ is the peak laser intensity along the z axis,

$$I_c=\left(1+\frac{4c^2}{r_0^2\omega_p^2}\right)\frac{P_0}{\pi c^2\tau_0^2(0)} \tag{15}$$

is a critical intensity, and $P_0=m^2c^5/|e|^2=8.71\,{\rm GW}$. A matched pulse in the longitudinal direction ($\partial T_0/\partial Z=0$, $T_0=1$) or soliton can exist only for $\beta_2<0$ and $I=I_c$. The variation of laser pulse duration has also been studied by others [34]. For short, broad pulses the nonlinear terms can be neglected, and only the GVD term remains. In this limit the envelope equation reduces to

$$\left(\frac{\partial^2}{\partial\tau^2}-\frac{2i}{\beta_2}\frac{\partial}{\partial z}\right)a(z,\tau)=0, \tag{16}$$

which is identical in form to the standard paraxial wave equation. For an initially Gaussian pulse, the longitudinal evolution is given by [31]

$$a(Z,\tau)=a_0\frac{1}{\sqrt{T_0(Z)}}\exp\left(-\frac{\tau^2}{\tau_0^2(o)T_0^2(Z)}\right)\exp[i\chi(Z,\tau)],$$

where $T_0(Z)=(1+Z^2)^{1/2}$ is the normalized pulse duration and

$$\chi(z,\tau)=\mathrm{sgn}(\beta_2)\left(-Z\frac{\tau^2}{\tau_0^2(z)}+\frac{1}{2}\tan^{-1}(Z)\right),$$

is the phase. The frequency chirp associated with the pulse is given by [31]

$$\delta\omega=-\partial\chi/\partial\tau=2\ \mathrm{sgn}(\beta_2)Z[\tau/\tau_0^2(0)T_0^2(Z)], \qquad (17)$$

where $\beta_2<0$ for a plasma. The frequency chirp varies linearly along the pulse and increases linearly with propagation distance.

IV. SIMULATION OF PULSE PROPAGATION IN CHANNELS

In this section we present numerical solutions of Eqs. (9a) and (9b), illustrating the characteristics of long and short pulses propagating in a plasma channel [10–17,35]. The channel radius is chosen such that it is initially matched to the part of the pulse containing the maximum power, i.e., $R_{\mathrm{ch}}=Z_R/\sqrt{1-P/P_p}$, where P is the peak laser power and $P_p[GW]=17.4(\lambda_p/\lambda)^2$ is the relativistic self-focusing power [see Eq. (22) and Ref. [14]]. Equations (9a) and (9b) are solved numerically on a Cartesian (x,y,z) grid. It is numerically expedient to transform away the cross derivative term in Eq. (9a). To this end Eq. (9a) is written in the form of a generalized nonlinear Schrödinger equation by expanding the operator

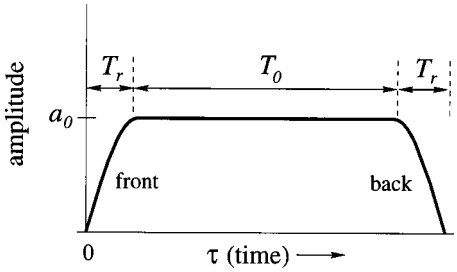

FIG. 2. Schematic diagram of the axial profile of the initial laser pulse.

$$\left(1+\frac{i}{k_0\nu_g}\frac{\partial}{\partial\tau}\right)^{-1}\approx\sum_{m=0}^{N}\left(-\frac{i}{k_0\nu_g}\frac{\partial}{\partial\tau}\right)^m,$$

where $\lambda/L\ll 1$ is the expansion parameter. A sufficient number of terms is kept to insure convergence; in the following illustrations $N=4$ is used. Nonparaxial contributions to the wave operator have been considered by others in numerical simulations [11,36]. The spatial profile of the electric field at $z=0$ is specified, and then propagated forward using a semi-implicit split-step method [31]. Linear terms in the wave equation representing GVD and transverse focusing effects are advanced in Fourier space. Consequently, the electric field must satisfy periodic axial and transverse boundary conditions. The remaining terms are handled in configuration (x,y,z) space by finite differencing the $\partial/\partial\tau$ and higher order derivatives. The equation for the density perturbation is solved at every step assuming that δn and its temporal derivatives are zero before the pulse.

The initial pulse profile is shown in Fig. 2, and is given by

$$a(r,0,\tau)=a_0\exp(-r^2/r_0^2)\begin{cases}\sin(\pi\tau/2T_r), & 0<\tau<T_r\\ 1, & T_r<\tau<T_0+T_r\\ \cos(\pi(\tau-T_0-T_r)/2T_r), & T_0+T_r<\tau<T_0+2T_r,\end{cases}$$

where T_r is the rise and decay time, and T_0 specifies the duration of the flat portion of the pulse

Long pulse

In this example the pulse duration is $\sim 5\tau_p$, where $\tau_p=2\pi/\omega_p$ is the plasma period ($T_0=5\tau_p$, $T_r=\tau_p/2$). The ambient plasma density is taken to be $n_0=1.24\times10^{18}\,\mathrm{cm}^{-3}$ ($\lambda_p=30\,\mu$m). The laser pulse has a wavelength $\lambda=1\,\mu$m and an initial spot size of 17.1 μm, corresponding to a Rayleigh length of 0.1 cm. The initial peak intensity is taken to be $I=3.4\times10^{17}\,\mathrm{W/cm}^2$ ($a_0=0.5$). The critical power for relativistic self-focusing is $P_p=15\,\mathrm{TW}$, while the peak laser power is 1.5 TW. Since the pulse power is well below P_p, the pulse would diffract within a few Rayleigh lengths in the absence of channel guiding. In the examples considered in this paper the laser power is chosen to be small compared with P_p to avoid nonlinear focusing effects [19]. The rise time is chosen so that a large density perturbation is generated and seeds the Raman instability. The growth rate of the conventional forward Raman instability [37] is $\Gamma=(a_0\omega_p^2)/(2\sqrt{2}\omega_0)$ which corresponds to an e-folding length of $\sim Z_R$ for these parameters.

Figures 3 and 4 show the $|a|^2$ and $\delta n/n_0$ profile along a planar cut through the center of the pulse ($y=0$) at $z=0$ and $z=5.5Z_R$. The pulse undergoes a Raman instability and is modulated at a period of $\sim\tau_p$. The profiles of the original pulse and wakefield are highly distorted as a result of this instability. Toward the back of the pulse, where the intensity is largest, some transverse self-focusing occurs, as shown in

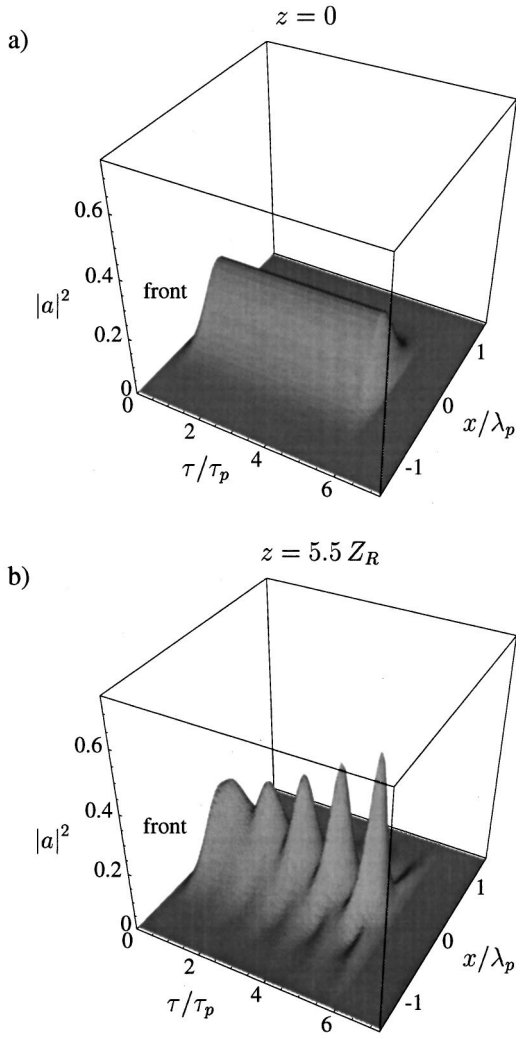

FIG. 3. Surface plots of the normalized intensity $|a|^2 = |e\mathbf{E}/mc\omega_0|^2$ on a planar cut through the center of the laser pulse ($y=0$) at $z=0$ and $z=5.5Z_R$. The parameters are $T_0=5\tau_p$, $T_r=\tau_p/2$, $n_0=1.24\times10^{18}\,\mathrm{cm}^{-3}$ ($\lambda_p=30\,\mu$m), $\lambda=1\,\mu$m, $r_0=17.1\,\mu$m, and $a_0=0.5$.

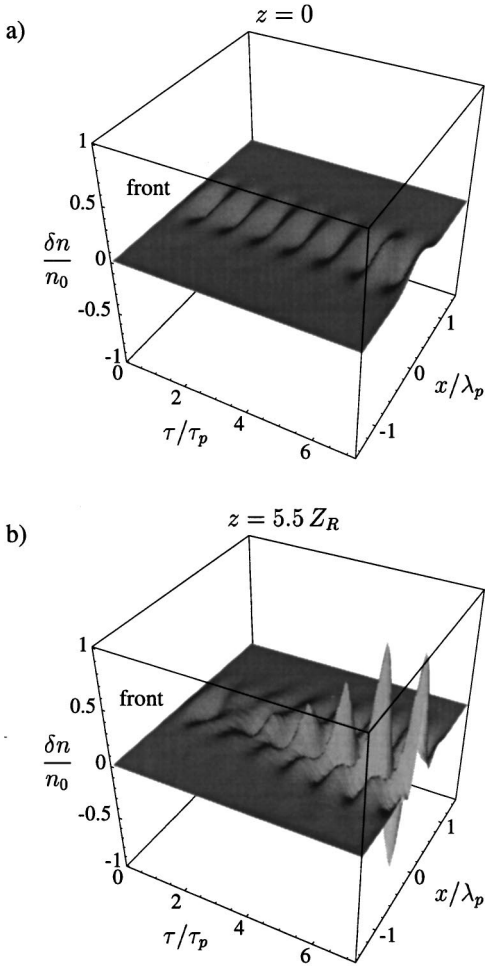

FIG. 4. Surface plots of the normalized density perturbation $\delta n/n_0$ at $z=0$ and $z=5.5Z_R$, corresponding to the pulse shown in Fig. 3.

Fig. 3(b). The wakefield amplitude shown in Fig. 4(b) varies within the pulse and has transverse structure. After propagating $5.5Z_R$, the normalized pulse intensity and density perturbation are large enough that the assumptions underlying the governing equations ($|a|<1, \delta n/n_0<1$) are no longer valid.

Figure 5 shows profiles of $|a|^2$ and the density perturbation along the pulse axis as a function of propagation distance. The modulations travel backwards in the group velocity frame. Figure 5(b) is a shaded contour plot of the on-axis density fluctuation as a function of τ and z. The amplitude of the density perturbation increases with propagation distance as the pulse is self-modulated. It should be noted that the wakefield has a phase velocity that is slower than the group velocity of the pulse [38,39].

Short pulse

In this example the pulse duration is $\sim\tau_p$, ($T_0=0$, $T_r=\tau_p/2$). Figure 6 shows a planar cut through the center of the pulse of the normalized intensity at $z=0$ and $z=30Z_R$. The pulse undergoes significant longitudinal compression and intensity gain due to modulation instability. The pulse compresses by a factor of ~2, while the intensity increases by ~2.4. After a distance $z=30Z_R$, the assumption that $|a|^2\ll1$, which underlies the propagation equation is violated. For $z<30Z_R$, the present simulation reproduces the results of an earlier 2D axis-symmetric simulation that is not limited to $|a|^2\ll1$.

The observed pulse compression and intensity gain are accompanied by an increase in the wakefield amplitude and by the generation of low frequency components within the pulse. Figure 7 shows the amplitude of the density perturbation on-axis at $z=0$ (dashed curve) and $z=30Z_R$ (solid curve). The wakefield density perturbation $\delta n/n_0$ increases due to the pulse distortion. Unlike in the previous example of Raman instability for a long pulse, no slippage of the wake relative to the pulse occurs. Figure 8 shows the Fourier transform of the electric field on axis initially and after propagating $30\,Z_R$. The spectrum broadens from $2\omega_p$ to $\sim6\omega_p$, while the dominant frequency component shifts downward by $\sim3\omega_p$.

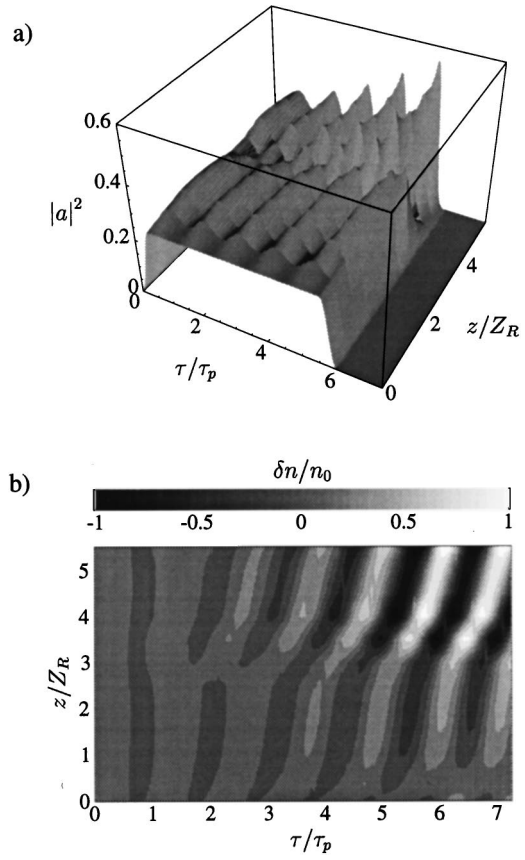

FIG. 5. Normalized on-axis ($r=0$) intensity (a) and density perturbation (b) as a function of τ/τ_p and the normalized propagation distance z/Z_R.

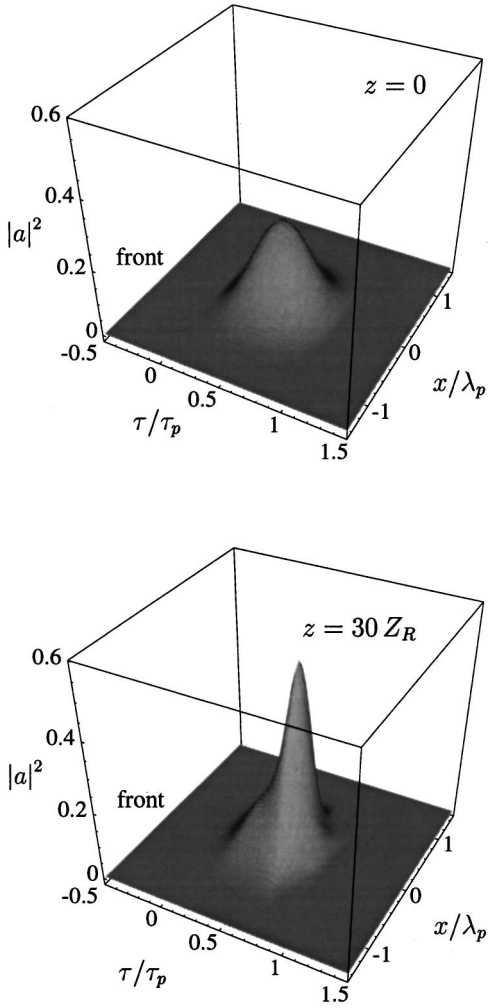

FIG. 6. Surface plots of the normalized intensity $|a|^2$ on a planar cut through the center of the laser pulse ($y=0$) at $z=0$ and $z=30Z_R$. The parameters are $T_0=0$, $T_r=\tau_p/2$, $n_0=1.24\times10^{18}\,\mathrm{cm}^{-3}$ ($\lambda_p=30\,\mu$m), $\lambda=1\,\mu$m, $r_0=17.1\,\mu$m, and $a_0=0.5$.

The conventional modulation instability (MI) is recovered from Eq. (9a) by considering an infinitely long beam that does not generate a density perturbation and hence, is not Raman unstable. The MI is unstable in the range of wave numbers between $k=0$ and $k=k_{\max}=a_0\omega_0/\sqrt{2}c$ with the maximum growth rate of $\Gamma_{\mathrm{MI}}=\omega_p^2a_0^2/8\omega_0$ occurring for $k=k_{\max}/\sqrt{2}$ [37]. A short pulse of length $L\leqslant\lambda_p$ is not unstable to Raman instability. However, it has an effective wave number $k=\pi/L$ and is subject to a modulation instability when $L>\pi/k_{\max}$. For parameters of the simulation, $L=21\pi/k_{\max}$, so that the effective wave number of the pulse is within the linearly unstable range and the maximum growth rate of the conventional MI corresponds to an e-folding length of $5Z_R$. Longitudinal compression and an increase in intensity of short pulses have also been reported by others [34].

V. GeV ELECTRON ACCELERATION IN A PLASMA CHANNEL

To utilize laser pulses for electron acceleration or radiation generation, it is necessary to propagate intense pulses many Rayleigh lengths in plasma without disruption. This can be accomplished by propagating a short pulse in a plasma channel. When the pulse length is shorter than a plasma wavelength, the density perturbation generated within the pulse tends to cancel the relativistic effects so that the pulse is stable to both modulation and Raman instabilities. In this parameter regime, group velocity dispersion can be minimized by making the dispersion length Z_{GVD}

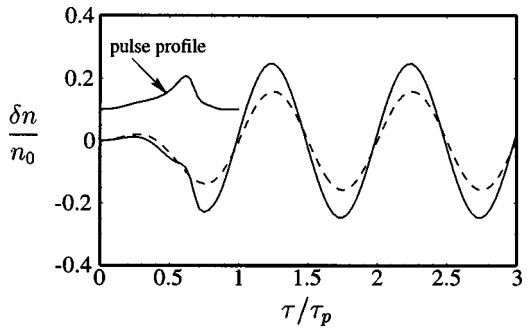

FIG. 7. Wakefield density variation $\delta n/n_0$ and $z=0$ (dashed curve) and $z=30Z_R$ (solid curve) associated with the laser pulse shown in Fig. 6. The intensity profile of the pulse at $z=30Z_R$ shows the location of the pulse relative to the wake.

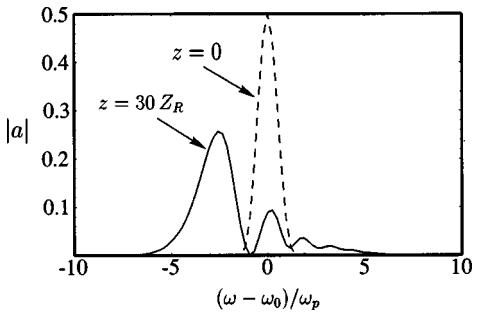

FIG. 8. On-axis electric-field spectrum at $z=0$ and $30Z_R$, associated with the laser pulse shown in Fig. 6.

$\cong \pi[\omega_0^2/(\omega_p^2+4c^2/r_0^2)]L^2/\lambda$ (L is the pulse length) much larger than the Rayleigh length. The effect is that the pulse can propagate undistorted over the long distances required for accelerator applications. Assuming that the pulse propagates undisrupted, the acceleration distance is limited by the dephasing length $L_d \approx \gamma_g^2 \lambda_p$, where $\gamma_g = \omega_0/\sqrt{\omega_p^2+4c^2/r_0^2}$. The electron energy gain is $\Delta W \cong \alpha |eE_{zo}| L_d$, where $E_{zo} \cong |\delta n/n_0| E_{\rm wb}/(1+8c^2/r_0^2\omega_p^2)$, $\alpha \cong \frac{1}{3}$ accounts for dephasing (slippage) and transverse focusing requirements, and $E_{\rm wb} = \omega_p mc/|e|$ is the wavebreaking field. An additional limitation on the acceleration distance in the channel-guided LWFA is the pulse energy depletion length, $L_e \cong |a|^2(\omega_0/\omega_p)^2(E_{\rm wb}/E_{z0})^2 L$.

An example of the extended propagation of a short pulse in a plasma channel is shown in Fig. 9. The parameters are $n_0 = 1.1\times 10^{17}\,{\rm cm}^{-3}$ ($\lambda_p = 100\,\mu$m), $\lambda = 2\pi c/\omega_0 = 1\,\mu$m, $r_0 = 70\,\mu$m, and $a_0 = 0.6$; $c\tau_0 = L = 37\,\mu$m is the pulse length; $Z_R = 1.5$ cm; $P_p = 174$ TW is the critical power for relativistic focusing [18]; $P = 38$ TW is the peak laser pulse power; $L_d = 55Z_R$; $Z_{\rm GVD} \cong 2300 Z_R$; and $L_e = 865 Z_R$. Figure 9 shows the laser intensity and corresponding density perturbation on a planar cut through the center of the pulse at $z=0$ and at $z=53Z_R$. Little distortion of the pulse or the wake is observed over this distance. In this example the peak wakefield is $|E_{zo}/E_{\rm wb}| \approx 0.1$, the peak perturbed density is $|\delta n/n_0| \approx 0.15$ and the estimated energy gain is $\Delta W = \alpha |eE_{z0}| L_d \cong 0.9$ GeV. In the following section, we show how tapering the plasma channel can increase this energy gain.

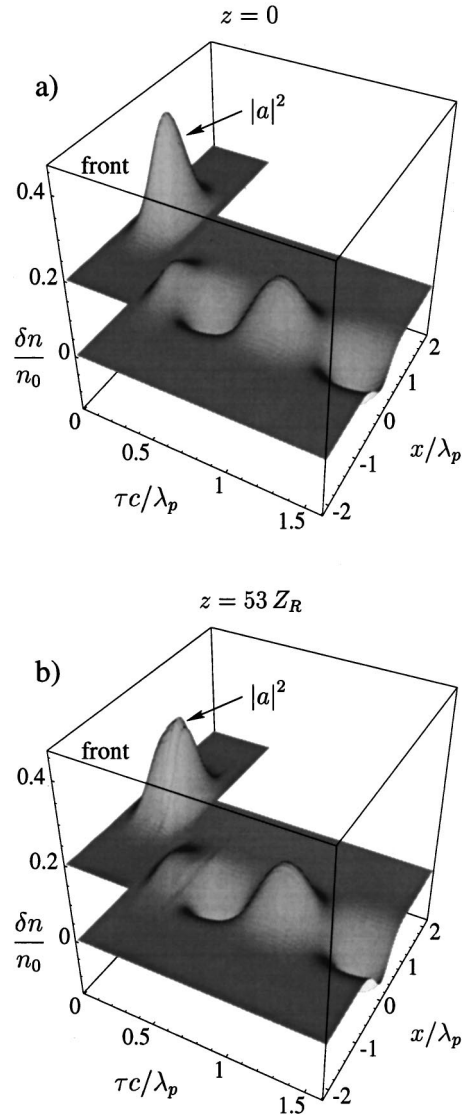

FIG. 9. Surface plots of the normalized intensity $|a|^2$ and density perturbation $\delta n/n_0$ on a planar cut through the center of the pulse for $\lambda = 1\,\mu$m, $\lambda_p = 100\,\mu$m, and $r_0 = 70\,\mu$m, at (a) $z=0$ and (b) $z=53Z_R$, where $|a(z=0)|^2_{\rm max} = 0.36$ and $|\delta n(z=0)/n_0|_{\rm max} = 0.15$.

VI. LWFA IN A TAPERED PLASMA CHANNEL

In this section the wakefield generated by a laser pulse in tapered plasma channel is analyzed. For this purpose the on-axis accelerating wakefield within and behind the laser pulse is obtained. The normalized electric field associated with the wakefield, from Eq. (2), is given by

$$\frac{\partial^2 \hat{\mathbf{E}}_p}{\partial \tau^2} + \omega_p^2(z)\hat{\mathbf{E}}_p = -\frac{c}{4\omega_p(0)}\omega_p^2(z)\nabla |a(r,z,\tau)|^2, \quad (18)$$

where $\hat{\mathbf{E}}_p = \mathbf{E}_p/E_{\rm wb}$, $E_{\rm wb} = (mc/|e|)\omega_p(0)$ is the wavebreaking field, and the perturbed plasma density, from Eq. (3), is

$$\frac{\delta n}{n_0(z)} = -\frac{\omega_p(0)}{c}\frac{c^2}{\omega_p^2(z)}\nabla\cdot\hat{\mathbf{E}}_p . \quad (19)$$

To solve for $\hat{\mathbf{E}}_p$ in Eq. (18), it is necessary to obtain the normalized field amplitude $a(r,z,\tau)$ in a tapered channel. This is accomplished by using a WKB solution of Eq. (8). Neglecting nonlinear terms, GVD, and terms of order $\lambda/c\tau_0$, Eq. (8) simplifies to

$$\left[\nabla_\perp^2 + \frac{4}{r_0^2} - \frac{\omega_p^2(z)}{c^2}\frac{r^2}{R_{\rm ch}^2(z)} + 2ik_0(z)\frac{\partial}{\partial z} + i\frac{\partial k_0(z)}{\partial z}\right] a(r,z,\tau) = 0. \quad (20)$$

For a matched laser pulse, i.e., a spot size r_0 independent of z, having a Gaussian radial profile

$$a(r,z,\tau)=A(z,\tau)\exp(-r^2/r_0^2), \tag{21}$$

we find that the channel radius is given by

$$R_{\rm ch}(z)=\frac{r_0^2}{2}\frac{\omega_p(z)}{c}. \tag{22}$$

The envelope equation for $A(z,\tau)$ becomes

$$\left(2k_0(z)\frac{\partial}{\partial z}+\frac{\partial k_0(z)}{\partial z}\right)A(z,\tau)=0, \tag{23}$$

with the solution

$$A(z,\tau)=A_0(\tau)[k_0(0)/k_0(z)]^{1/2}. \tag{24}$$

Using Eq. (21) together with Eq. (24), the normalized axial electric field, within the laser pulse is given by

$$\hat{E}_{p,z}(r=0,z,\tau)\cong-\frac{\omega_p(z)}{4\omega_p(0)}\frac{k_0(0)}{k_0(z)}\frac{c}{\nu_g(z)}\times\int^{\tau}\frac{\partial A_0^2(\tau')}{\partial\tau'}\sin[\omega_p(z)(\tau'-\tau)]d\tau', \tag{25}$$

where ∂/∂_z has been approximated by $-\nu_g^{-1}\partial/\partial\tau$. The axial field behind the pulse is obtained from the homogeneous solution of Eq. (25) together with the appropriate continuity conditions at the back of the pulse, $\tau=\tau_0$. The laser pulse is taken to have the envelope

$$A_0(\tau)=a_0\sin(\pi\tau/\tau_0), \tag{26}$$

for $0\leqslant\tau\leqslant\tau_0$, and zero otherwise. Note that the front of the pulse is at $\tau=0$ while the back of the pulse is located at $\tau=\tau_0$. Substituting Eq. (26) into (25), the axial component of the wakefield within the pulse $(0\leqslant\tau\leqslant\tau_0)$ is

$$\hat{E}_{p,z}(r=0,z,\tau)=-E_0(z)\{\sin[\omega_p(z)\tau]-(\omega_p(z)\tau_0/2\pi)\sin(2\pi\tau/\tau_0)\}, \tag{27a}$$

and behind the pulse $(\tau\geqslant\tau_0)$ is

$$\hat{E}_{p,z}(r=0,z,\tau)=-2E_0(z)\sin(\omega_p(z)\tau_0/2)\times\cos[\omega_p(z)(\tau-\tau_0/2)], \tag{27b}$$

where

$$E_0(z)=\frac{a_0^2}{8}\frac{\omega_p(z)}{\omega_p(0)}\frac{k_0(0)}{k_0(z)}\frac{c}{\nu_g(z)}\frac{(2\pi/\tau_0)^2}{[\omega_p^2(z)-(2\pi/\tau_0)^2]}. \tag{28}$$

The phase of the axial component of the wakefield behind the laser pulse is $\psi(z,\tau)=\omega_p(z)(\tau-\tau_0/2)$. In the laboratory frame the frequency and wave number associated with the phase of the accelerating wave are

$$\Omega(z)\equiv\frac{\partial\psi(z,\tau)}{\partial\tau}=\omega_p(z), \tag{29a}$$

$$K(z,\tau)\equiv-\left(\frac{\partial}{\partial z}-\frac{1}{\nu_g(z)}\frac{\partial}{\partial\tau}\right)\psi(z,\tau)=\frac{\omega_p(z)}{\nu_g(z)}\left(1-\frac{\partial\omega_p(z)}{\partial z}(\tau-\tau_0/2)\right). \tag{29b}$$

respectively. Using Eqs. (29), the standard definition for the phase velocity, $\nu_{\rm ph}$, yields

$$\nu_{\rm ph}(z,\tau)\equiv\frac{\Omega(z,\tau)}{K(z,\tau)}=\frac{\nu_g(z)}{\{1-[\partial\omega_p(z)/\partial z][\nu_g(z)/\omega_p(z)](\tau-\tau_0/2)\}}. \tag{30}$$

Expressions similar to Eqs. (29) and (30) were applied by Bulanov *et al.* [23] to examine the variation of the phase velocity for a particular density profile. Here we make use of Eqs. (29) and (30) to determine the precise form of the density tapering required to achieve optimal acceleration. The wavelength associated with the wakefield is $\lambda_w(z,\tau)=2\pi/K(z,\tau)$, where K is given by Eq. (29b), and is a function of z and τ for a tapered plasma density. The phase velocity of the wakefield increases (decreases) with distance from behind the pulse for an increasing (decreasing) plasma density. The location behind the pulse, τ_c, for which the phase velocity equals the speed of light in vacuum is given by

$$\tau_c(z)=\left(\frac{1}{2}\frac{\omega_p^2}{\omega_0^2}+\frac{2c^2}{\omega_0^2r_0^2}\right)\Big/\left(c\frac{\partial\ln\omega_p}{\partial z}\right)+\frac{\tau_0}{2}. \tag{31}$$

In general τ_c is a function of z and τ, and as the laser pulse propagates the location behind the pulse for which $\nu_{\rm ph}=c$, i.e., the luminous point, moves relative to the back of the pulse. The existence of a luminous point behind the laser pulse was noted in an earlier wakefield simulation [40].

For the luminous point to remain fixed relative to the wakefield, say N plasma wavelengths behind the pulse, the plasma density taper must satisfy

$$\partial\hat{\omega}_p/\partial\hat{z}=(\hat{\omega}_p^2/2\pi N)[(\pi r_0/\lambda)^2\hat{\omega}_p^2+1], \tag{32}$$

where $\hat{\omega}_p=\omega_p(\hat{z})/\omega_0$, $\lambda=2\pi c/\omega_0$, and $\hat{z}=z/Z_R$.

The solid curve in Fig. 10 shows the numerical solution of Eq. (32) for $N=1.5$, and with the same parameters used in Fig. 9. In Fig. 10, the plasma period is normalized to the initial pulse duration. To facilitate the fully numerical solution of Eqs. (2) and (8), an analytical form for $\omega_p(z)$ is used;

$$\omega_p(z)=\omega_p(0)\exp\left(\sum_{j=1}^{4}\alpha_j\hat{z}^j\right),$$

where α_j are the fitting constants. The dashed curve in Fig. 10 represents a best fit to the numerical solution using the

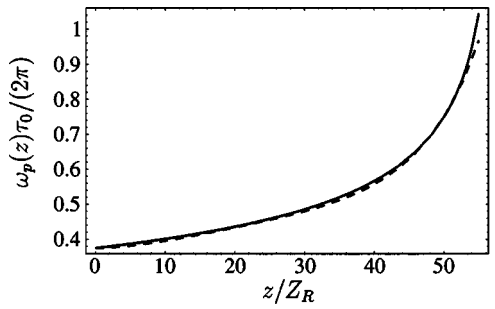

FIG. 10. Solution of Eq. (32) showing the normalized plasma frequency as a function of z/Z_R, for $N=1.5$, $r_0=0.7\lambda_p$, $\omega_0/\omega_{po}=100$, $a_0=0.6$, and $c\tau_0=0.37\lambda_p$. The dashed curve denotes the analytic form for ω_p used in the numerical simulations discussed in the text.

analytic form. To provide guiding, the plasma channel radius varies as indicated by Eq. (22).

The plasma density in Fig. 10 increases such that, after a distance of $\sim 50Z_R$, the short pulse requirement ($\tau_0 < 2\pi/\omega_p$) breaks down and pulse distortion occurs as shown in Fig. 11. The curves in Fig. 11 represent the scaled on-axis laser intensity at $z=0$ and $z=52Z_R$ resulting from a numerical solution of Eqs. (2) and (8). The pulse distortion shown in Fig. 11 is not described by the WKB solution given by Eqs. (21) and (24), and is similar to that shown in Fig. 6 in which $\tau_0=2\pi/\omega_p$.

The energy gain of a test particle in the wake of the laser pulse ($\tau > \tau_0$) is obtained by solving the following coupled equations for the relativistic factor γ and the wake phase Ψ at the position of the particle,

$$\frac{\partial \gamma}{\partial z} = 2E_0(z)\sin[\omega_p(z)\tau_0/2]\cos\Psi, \tag{33a}$$

$$\Psi = \Psi|_{z_0} + \frac{\omega_p(z)}{c}\int_{z_0}^{z} dz\left[\frac{1}{\sqrt{1-1/\gamma^2}} - \frac{1}{\beta_g(z)}\right], \tag{33b}$$

where z_0 is the initial position of the particle.

Figure 12 shows the normalized on-axis longitudinal electric field, $\hat{E}_{p,z}$ $(r=0,z,\tau)$, as a function of $\tau c/\lambda_p$ $(z=0)$ and scaled propagation distance z/Z_R. Panel (a) shows the analytical solution given by Eqs. (27a), (27b), and (28). The white dashed curve denotes the trajectory of a test particle obtained from solving Eqs. (33) with the analytic wakefields. The particle is injected into the luminous part of the wake and remains in an accelerating and focusing region. Panel (b) shows the longitudinal electric field resulting from the full numerical calculation. Initially ($z/Z_R \leqslant 20$), oscillations occur due to the slight mismatch between the laser pulse and the channel. The luminous accelerating region, however, is preserved and evolves in a manner similar to the analytic model.

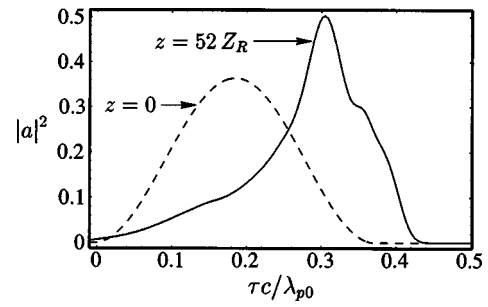

FIG. 11. Numerical simulations showing the on-axis profiles of the scaled intensity at $z=0$ (dashed curve) and $z=52Z_R$ (solid curve) for a pulse propagating in a tapered channel in which the plasma frequency is given by the dashed curve in Fig. 10. The other parameters are the same as for Fig. 9.

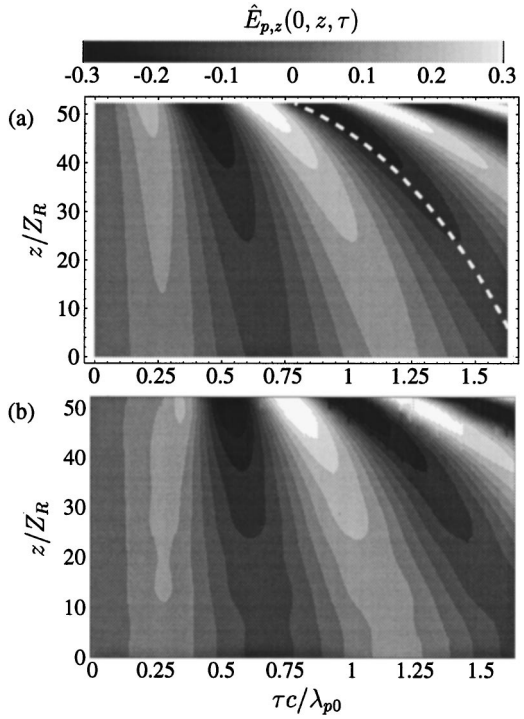

FIG. 12. (a) Normalized on-axis longitudinal electric field as a function of the propagation distance z/Z_R and time $\tau c/\lambda_{p0}$ obtained using the analytic model. (b) The full numerical simulation. Here $\lambda_{po}\equiv\lambda_p$ $(z=0)$. The parameters are the same as used in Fig. 11. The white, dashed curve in panel (a) denotes the trajectory of a test particle injected into the luminous part of the wake.

The solid curve in Fig. 13 shows the test particle energy

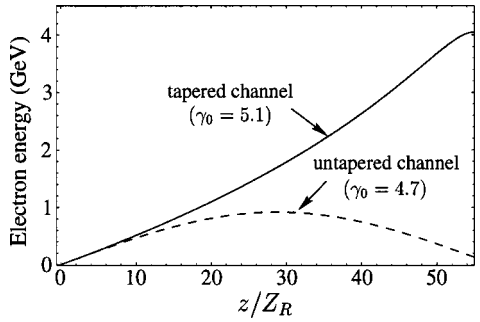

FIG. 13. The solid curve denotes the electron energy vs propagation distance for the test particle trajectory shown in Fig. 12(a). The dashed curve shows the energy obtained using an untapered channel.

as a function of propagation distance corresponding to the trajectory in Fig. 12(a). The dashed curve shows the solution obtained for an untapered channel. The predicted energy gain of 4 GeV is four times larger than the gain obtained using an untapered channel. Note also the dephasing length is larger in the tapered channel.

In an experimental realization of a tapered plasma channel the density can be tailored to closely follow the analytical form given by Eq. (32), with small variations due to voltage jitter, noise, etc. To quantify the role of the density variations we have investigated the effects of density profile perturbations on the energy gain. As an example we assume that the plasma frequency is given by $\omega_p(z)=\omega_{p0}(z)\lfloor+\varepsilon\sin(z/L_p)\rfloor$, where $\omega_{p0}(z)$ is a solution of Eq. (32), and ε and L_p are the amplitude and scale length of the perturbation, respectively. For the example shown in Fig. 11, we find that, for $\varepsilon\leqslant 0.1$ and for a broad range of $L_p(L_d/100<L_p<100L_d)$, the energy gain is not significantly diminished ($\sim$3.5 GeV).

Realization of tapered plasma channels

Capillary discharges are ideally suited for generating variable density plasma channels. In its simplest form, the device consists of a thin hollow cylinder of insulating material such as polyethylene with high voltage electrodes at the ends, and a plasma column is produced from wall material when an appropriate voltage pulse is applied. Capillary discharges have been used extensively to generate plasma columns with the on-axis density minimum required for optical guiding of intense laser pulses. High efficiency transmission over distances of several centimeters was demonstrated in several experiments [25–27], with guided laser spot sizes of 20–30 μm. Hydrodynamic simulations of capillary discharges [27] indicate that the on-axis plasma density n_0 increases with the discharge current I_d or voltage V_d and scales as R_c^{-3}, where R_c is the radius of the capillary. This suggests that plasma density can be varied by changing the channel radius or discharge current or voltage along the capillary. Control of the plasma density by tapering the channel radius was demonstrated in Ref. [27]. Plasma densities at each end of the capillary were deduced from interferometry measurements. A 2-cm-long capillary with diameter tapered from 300 to 500 μm showed a factor of 2 drop in the on-axis plasma density. A similar capillary with a 500–1400-μm taper exhibited a density reduction of more than an order of magnitude, with N_e going from 10^{19} to $8\times10^{17}\,\mathrm{cm}^{-3}$. Results were consistent with one-dimensional hydrodynamic simulations.

Other experiments demonstrated an alternative approach that produces an axial variation in the channel density by varying the discharge current I_d. This is accomplished by dividing the capillary into separate segments, each connected to a separate capacitor that can be charged to a different voltage. An experimental demonstration of the segmented capillary technique was carried out using a three stage, 0.5-mm-diameter capillary and a Ti sapphire laser at 800 nm, producing 40 mJ in a 160-fs-long pulse with a pulse repetition rate of 10 Hz. The group velocity of the laser pulse propagating through a single stage of the capillary was measured using an autocorrelator, thus providing a direct measure of the plasma density. Raman backscatter provided an additional density diagnostic.

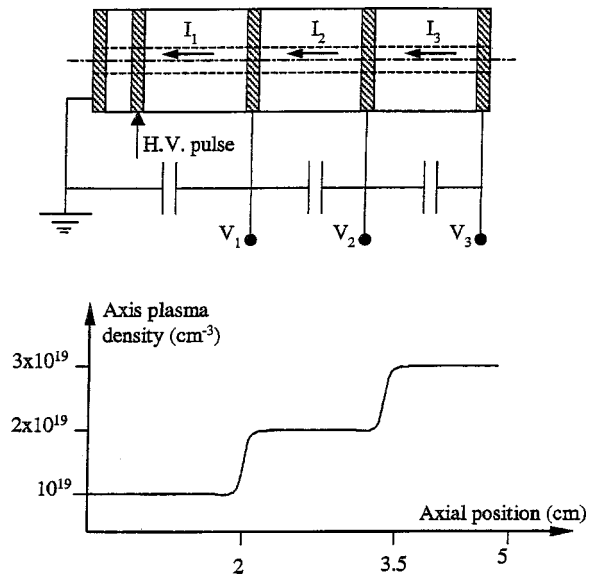

FIG. 14. A segmented capillary discharge that produces an axial variation in the plasma density. The top portion of the figure illustrates the configuration for a three-stage segmented capillary. A typical axial plasma density profile is shown at the bottom portion of the figure for $V_1<V_2<V_3$.

The top part of Fig. 14 illustrates the configuration for a three stage segmented capillary. A typical axial plasma density profile is shown in the bottom portion of the figure for a case with $V_1<V_2<V_3$. The plasma density is expected to be approximately constant in each segment, as shown in the figure. Since the capillary diameter remains the same in each segment, the guided laser spot size should be nearly constant throughout the capillary, thus preserving the high intensity required for wakefield generation.

VII. CONCLUSIONS

This paper presents an analysis of intense laser pulse propagation in a plasma channel. The results of this study are relevant to a number of areas including laser wakefield acceleration and x-ray laser development. The analysis is based on a coupled pair of equations for the laser and the plasma electric fields and includes the effects of 3D and nonparaxial propagation, group velocity dispersion, relativistic mass variation, and a tapered plasma channel. It is shown that propagation of short and long pulses can be markedly different. For a pulse that is long compared to a plasma wavelength, Raman, and modulational instability lead to pulse breakup and disruption after a few Rayleigh ranges. On the other hand, for pulses that are short compared to a plasma wavelength, extended propagation is demonstrated. It is shown that for broad, short pulses the Raman and modulational instability terms in the wave equation cancel out. In this limit, laser propagation of a laser pulse is only limited by pulse dispersion. For an up-tapered plasma channel it is

shown that the phase velocity of the wakefield behind the laser pulse increases with distance from the back of the pulse. Several wavelengths behind the pulse the wake phase velocity can equal the speed of light vacuum. Finally, wakefields in a tapered plasma have been numerically simulated. In a tapered channel, the dephasing distance is increased relative to the untapered channel, and larger energy gains are achieved.

ACKNOWLEDGMENTS

This work was supported by the Department of Energy and the Office of Naval Research.

[1] P. Sprangle, E. Esarey, A. Ting, and G. Joyce, Appl. Phys. Lett. **53**, 2146 (1988).
[2] E. Esarey, P. Sprangle, J. Krall, and A. Ting, IEEE Trans. Plasma Sci. **24**, 252 (1996).
[3] A. Modena, Z. Najmudin, A. E. Dangor, C. E. Clayton, K. A. Marsh, C. Joshi, V. Malka, C. B. Darrow, and C. Danson, IEEE Trans. Plasma Sci. **24**, 289 (1996).
[4] C. I. Moore, A. Ting, K. Krushelnick, E. Esarey, R. F. Hubbard, B. Hafizi, H. R. Burris, C. Manka, and P. Sprangle, Phys. Rev. Lett. **79**, 3909 (1997); E. Esarey, B. Hafizi, R. Hubbard, and A. Ting, *ibid.* **80**, 5552 (1998).
[5] D. Gordon, K. C. Tzeng, C. E. Clayton, A. E. Dangor, V. Malka, K. A. Marsh, A. Modena, W. B. Mori, P. Muggli, Z. Najmudin, D. Neely, C. Danson, and C. Joshi, Phys. Rev. Lett. **80**, 2133 (1998).
[6] D. Umstadter, S. Y. Chen, A. Maksimchuk, G. Mourou, and R. Wagner, Science **273**, 472 (1996).
[7] F. Dorchies, J. R. Marques, B. Cros, G. Matthieussent, C. Courtois, T. Velikoroussov, P. Audebert, J. P. Geindre, S. Rebibo, G. Hamoniaux, and F. Amiranoff, Phys. Rev. Lett. **82**, 4655 (1999).
[8] E. Esarey, P. Sprangle, J. Krall, and A. Ting, IEEE Trans. Plasma Sci. **33**, 1879 (1997).
[9] P. Chessa, P. Mora, and T. M. Antonsen, Phys. Plasmas **5**, 3451 (1998).
[10] T. M. Antonsen and P. Mora, Phys. Fluids B **5**, 1440 (1993).
[11] P. Mora and T. M. Antonsen, Phys. Plasmas **4**, 217 (1997).
[12] C. D. Decker and W. B. Mori, Phys. Rev. Lett. **72**, 490 (1994); Phys. Rev. E **51**, 1364 (1995).
[13] W. B. Mori, IEEE J. Quantum Electron. **33**, 1942 (1997).
[14] P. Sprangle, B. Hafizi, and J. R. Penano, Phys. Rev. E **61**, 4381 (2000).
[15] P. Sprangle, J. Krall, and E. Esarey, Phys. Rev. Lett. **73**, 3544 (1994).
[16] B. J. Duda and W. B. Mori, Phys. Rev. E **61**, 1683 (2000).
[17] P. Sprangle and B. Hafizi, Phys. Plasmas **6**, 1683 (1999).
[18] A. B. Borisov, A. V. Borovskiy, O. B. Shiryaev, V. V. Korobkin, A. M. Porokhorov, J. C. Solem, T. S. Luk, K. Boyer, and C. K. Rhodes, Phys. Rev. A **45**, 5830 (1992); B. Hafizi, A. Ting, P. Sprangle, and R. F. Hubbard, Phys. Rev. E **62**, 4120 (2000).
[19] P. Sprangle, B. Hafizi, and P. Serafim, Phys. Rev. Lett. **82**, 1173 (1999); Phys. Rev. E **59**, 3614 (1999).
[20] E. Esarey, C. B. Schroeder, B. A. Shadwick, J. S. Wurtele, and W. P. Leemans, Phys. Rev. Lett. **84**, 3081 (2000).
[21] N. E. Andreev, L. M. Gorbunov, and A. A. Frolov, Fiz. Plazmy **24**, 888 (1998) [Plasma Phys. Rep. **24**, 825 (1998)].
[22] N. E. Andreev, L. M. Gorbunov, V. I. Kirsanov, K. Nakajima, and A. Ogata, Phys. Plasmas **4**, 1145 (1997).
[23] S. Bulanov, N. Naumova, F. Pegoraro, and J. Sakai, Phys. Rev. E **58**, R5257 (1998).
[24] K. Krushelnick, A. Ting, C. I. Moore, H. R. Burris, E. Esarey, P. Sprangle, and M. Baine, Phys. Rev. Lett. **78**, 4047 (1997).
[25] Y. Ehrlich, C. Cohen, D. Kaganovich, A. Zigler, R. F. Hubbard, P. Sprangle, and E. Esarey, J. Opt. Soc. Am. B **15**, 2416 (1998).
[26] D. Kaganovich, A. Ting, C. I. Moore, A. Zigler, H. R. Burris, Y. Ehrlich, R. Hubbard, and P. Sprangle, Phys. Rev. E **59**, R4769 (1999).
[27] D. Kaganovich, P. Sasorov, C. Cohen, and A. Zigler, Appl. Phys. Lett. **75**, 772 (1999).
[28] C. G. Durfee III and H. M. Milchberg, Phys. Rev. Lett. **71**, 2409 (1993); C. G. Durfee III, J. Lynch, and H. M. Milchberg, Phys. Rev. E **51**, 2368 (1995); C. G. Durfee III, T. R. Clark, and H. M. Milchberg, J. Opt. Soc. Am. B **13**, 59 (1996).
[29] H. M. Milchberg, T. R. Clark, C. G. Durfree, T. M. Antonsen, and P. Mora, Phys. Plasmas **3**, 2149 (1996).
[30] P. Volfbeyn, E. Esarey, and W. P. Leemans, Phys. Plasmas **6**, 2269 (1999).
[31] G. P. Agrawal, *Nonlinear Fiber Optics* (Academic, San Diego, CA, 1995).
[32] P. Sprangle, E. Esarey, and A. Ting, Phys. Rev. A **41**, 4463 (1990).
[33] C. A. Kapetanakos, B. Hafizi, H. M. Milchberg, P. Sprangle, R. Hubbard, and A. Ting, IEEE J. Quantum Electron. **QE-35**, 565 (1999).
[34] C. Ren, B. J. Duda, R. G. Hemker, W. B. Mori, T. Katsouleas, T. M. Antonsen, Jr., and P. Mora, Phys. Rev. E **63**, 026411 (2001).
[35] R. F. Hubbard, P. Sprangle, and B. Hafizi, IEEE Trans. Plasma Sci. **28**, 1159 (2000); R. F. Hubbard, D. Kaganovich, B. Hafizi, C. I. Moore, P. Sprangle, A. Ting, and Z. Zigler, Phys. Rev. E **63**, 036502 (2001).
[36] J. Krall, E. Esarey, P. Sprangle, and G. Joyce, Phys. Plasmas **1**, 1738 (1994).
[37] P. Sprangle, E. Esarey, and B. Hafizi, Phys. Rev. Lett. **79**, 1046 (1997); Phys. Rev. E **56**, 5894 (1997).
[38] W. P. Leemans, C. W. Siders, E. Esarey, N. E. Andreev, G. Shvets, and W. B. Mori, IEEE Trans. Plasma Sci. **24**, 331 (1996).
[39] N. E. Andreev, V. I. Kirsanov, L. M. Gorbunov, and A. S. Sakharov, IEEE Trans. Plasma Sci. **24**, 331 (1996).
[40] T. Katsouleas, Phys. Rev. A **33**, 2056 (1986).